



Enhanced irradiation tolerance of a medium entropy alloy via precipitation and dissolution of nanoprecipitates

Jihong Han^a, Yang Zhang^{a,*}, Zhiyan Sun^b, Yunfei Zhang^b, Yingli Zhao^b, Lixin Sun^a, Zhongwu Zhang^{a,^{*}}

^a Key Laboratory of Superlight Materials and Surface Technology, Ministry of Education, College of Materials Science and Chemical Engineering, Harbin Engineering University, Harbin 150001, China

^b HBIS Materials Technology Research Institute, HBIS Group, Shijiazhuang, Hebei 050000, China



ARTICLE INFO

Keywords:

Medium entropy alloy
Radiation damage
Nanoprecipitates
Mechanical properties
Swelling

ABSTRACT

High/medium entropy alloys (HEAs/MEAs) are good candidates for nuclear applications due to the excellent mechanical properties, good corrosion resistance and radiation resistance. In this work, a novel cobalt-free MEA was developed by introducing L1₂ nanoprecipitates. The microstructure evolution and radiation tolerance were evaluated after bombarded using 3 MeV Fe¹¹⁺ ions at 500 °C. The evolution of nanoprecipitates was closely related to the irradiation dose, and dominated by irradiation-enhanced diffusion and ballistic dissolution mechanism. For the solid-solution MEA (without L1₂ nanoprecipitates), irradiation hardening occurred due to the irradiation-induced formation of precipitates, voids and dislocation loops. However, in MEA with L1₂ nanoprecipitates after aging, irradiation induced dissolution and reprecipitation of nanoprecipitates were observed. Different from the solid-solution MEA, the hardness kept almost unchanged in the aging sample after irradiation. The swelling rate of the solid-solution sample after irradiation is 9.4×10^{-6} %/dpa, while no swelling occurs in the aging sample under the same irradiation condition. Besides, the average size and number density of dislocation loops in the aging sample decreased by ~ 40% and ~ 28%, compared with the solid-solution sample. The precipitation and dissolution of nanoprecipitates substantially improved the radiation tolerance of the cobalt-free MEA.

1. Introduction

The defects, such as dislocation loops [1,2], voids/bubbles [3,4] or brittleness precipitation [5–8] caused by cascading damage will greatly affect the stability of mechanical properties, and then lead to embrittlement or even failure of materials [9,10]. In previous studies, the basic strategy for designing structural materials with good radiation tolerance is to inhibit the growth and accumulation of defects in materials [11–15]. For example, the irradiation tolerance of nanocrystalline tungsten was higher than that of coarse-grained tungsten, and the formation of helium bubbles in nanocrystalline tungsten was effectively inhibited even after the increase of nearly two orders of magnitude in irradiation dose [12]. However, advanced nuclear energy systems have put forward higher requirements for structural materials. Unfortunately, austenitic steels with swelling rate of 0.1 ~ 2.5% cannot show sufficient radiation tolerance under the condition of irradiation at 450 ~ 700 °C

and ~ 10 dpa [16–18]. Therefore, the widely used austenitic steels have been unable to operate in the complex environment of the next generation nuclear energy system for a long time [13,16,19,20].

In recent years, HEAs/MEAs have attracted great attention from researchers owing to their unique compositions, excellent mechanical properties and good radiation tolerance, and are considered as potential candidates to meet the application conditions of next-generation nuclear energy systems [19,21–24]. Current studies have shown that with the increase of the number of principal elements, the accumulation of radiation damage in HEAs/MEAs is inhibited, and the high level of lattice distortion and composition complexity in HEAs/MEAs can change the energy dissipation process and promote the recovery of radiation damage in the early stage of irradiation [4,15,25,26]. Therefore, compared with pure nickel, the migration rate, damage accumulation and evolution of defect clusters are significantly delayed [4,15,21,26]. In addition, by controlling the type and number of main elements in HEAs/MEAs,

* Corresponding authors.

E-mail addresses: zhangyang0115@hrbeu.edu.cn (Y. Zhang), zwzhang@hrbeu.edu.cn (Z. Zhang).

radiation swelling can be significantly inhibited [4,15,25]. For example, Jin et al. [4] found that the swelling rate of NiCoFe was much lower than that of NiCoCr. The swelling rate of NiCoFeCr ($\sim 0.02\%$) is more than one order of magnitude lower than that of NiCo alloy ($\sim 0.42\%$) [21]. Furthermore, adding Mn to NiCoFeCr can further reduce the swelling rate and make the swelling resistance ~ 40 times higher than that of pure nickel [4]. However, compared to NiCoFeCrMn, NiCoFeCrPd showed stronger inhibition of swelling at high temperatures [27]. Moreover, irradiation-induced redistribution of alloying elements may lead to precipitation in HEAs/MEAs [19,28–31]. For example, the brittle L₁₀ (NiMn) phases were precipitated after electron irradiation at 1 dpa at 400 °C in CrFeCoNiMn and CrFeCoNiPd HEAs, which were controlled by mixing enthalpy [32]. However, irradiation of Kr²⁺ ions at 500 °C and ~ 1 dpa can significantly promote the formation of the strengthening precipitates (L₁₂ precipitates) in Al_{0.3}CoCrFeNi [30]. The irradiation enhanced diffusion drives alloying elements to break away from solid solutions and form precipitates, which accelerates the formation of precipitates compared with equilibrium heat treatment [19,28–32]. Previous studies have shown that the addition of cobalt to HEAs/MEAs can promote the precipitation of L₁₂ precipitates and improve its stability, which is conducive to regulating the size and number density of L₁₂ precipitates [33–35]. The pre-existing precipitates in HEAs/MEAs will gradually shrink and even dissolve under the action of accelerating atomic diffusion caused by irradiation, resulting in phase instability [28, 31,36]. For example, the pre-existing L₁₂ precipitates in the FeCoNiCr-based HEAs tend to shrink gradually from their surface with increasing dose [31,36]. In general, the evolution of irradiation-induced precipitates is thought to be controlled by two competing factors, enhanced diffusion and displacement damage [31,36]. Irradiation can induce reprecipitation while inducing shrinkage [31]. Therefore, keeping the number density of nanoprecipitates constant under the control of two competing factors is the key to controlling the stability of microstructure.

Irradiation precipitation/dissolution will undoubtedly affect the hardness of the alloy [37,38]. However, in HEAs/ MEAs, high density dislocation loops are retained due to lattice distortion and compositional complexity [15,26], resulting in significant irradiation hardening [4,15, 26,39]. For example, under irradiation with Xe³⁺ ions of $\sim 10^{16}$ ions /cm², the hardness of NiCoCrFePd HEA increases by 57%, which is mainly due to the contribution of dislocation loops [40]. After irradiation by Xe²³⁺ ion with 3.8 dpa at room temperature, the hardening rate of the Fe₃₈Mn₄₀Ni₁₁Al₄Cr₇ HEA reached 66% [41]. It has been found that the precipitation and dissolution transformation of nanoprecipitates in martensitic steel and CoCrFeNi-based HEAs controlled by two competing factors, enhanced diffusion and displacement damage, can reduce the size of dislocation loops [31,42,43]. For example, Cao et al. [43] used this method to control the density of the dislocation loops to $6.9 \times 10^{14} \text{ m}^{-2}$ and limit the maximum size of the loops to 26 nm. However, how to control the number densities of nanoprecipitates and dislocation loops to maintain the hardness constant is still unknown, especially in cobalt-free HEAs/MEAs. Current studies on irradiation response and defect evolution of HEAs/MEAs mostly focus on traditional systems, such as FeCoCrMnNi, FeCoCrNi, NiCoCr and FeCoCrNiAl [26, 27,32]. In addition to the high price of cobalt, which restricts its commercialization [44–46], highly activated cobalt is radioactive after irradiation, and the initial materials usually contain no cobalt or only trace cobalt [16,47]. Most importantly, the L₁₂ nanoprecipitates in the cobalt-free HEAs/MEAs cannot be promoted by cobalt and its stability will be greatly weakened, so that the above problems cannot be solved to a certain extent. Therefore, the development of new low-cost radiation-resistant cobalt-free HEAs/MEAs is urgent. It is of great significance to study the effect of nanoprecipitates on the irradiation tolerance of cobalt-free HEAs/MEAs.

In this study, the microstructure and hardness variations of the solid-solution and aging MEAs under high-temperature and high-dose irradiation were evaluated. The evolution of nanoprecipitates and their

effects on radiation tolerance were revealed. The precipitation and dissolution of nanoprecipitates on the mechanisms of swelling and hardness variation were also discussed detailedly.

2. Experiment

The MEA with composition of Cr₂₀Fe₃₂Ni₃₅Mo₃Al₇Nb₃ (at%) was designed. As mentioned in the introduction, irradiation precipitation in HEAs/MEAs is affected by the enthalpy of mixing. Therefore, in the design of alloy composition, Ni, Al and Nb elements with low mixing enthalpy [48] (Ni-Al is 29 kJ/mol, Ni-Nb is 30 kJ/mol) are selected to form L₁₂ nanoprecipitates to improve the strength or hardness [34,45, 49]. Fan et al. [50] found that the addition of Nb element in HEA played a role in promoting the precipitation of L₁₂ nanoprecipitates. Therefore, the content of Ni, Al and Nb is 35 at.%, 7 at.% and 3 at.%, respectively. In theory, the enthalpy of mixing of Co with other elements in CrMnFeCoNi, CoCrFeNi, CrCoNi HEAs/MEAs is relatively small (Co-Cr is 4 kJ/mol, and Co-Mn is 5 kJ/mol) [48]. In addition, from the valence electron concentration (VEC) criterion [51], the content of Co (VEC = 9) is between 20 and 33 at.%, which makes it more conducive to driving the VEC ≥ 8.0 of CrMnFeCoNi, CoCrFeNi, FeCoNi, CrCoNi HEAs/MEAs, thus promoting the formation of face-centered cubic (FCC) matrix. The study of Laplanche and Wu et al. [52,53] confirmed that all the above four HEAs/MEAs were FCC structures. However, the CrFeNi MEA with the removal of Co elements also ensures that VEC = 8.0, and the FCC single-phase structure is still in the solid solution state, but the Cr-rich body-centered cubic (BCC) phase precipitated by annealing for a short time below the solution temperature has an adverse effect on the mechanical properties of the alloy [54,55]. Therefore, in order to ensure the microstructure stability under annealing or irradiation, the contents of Fe and Ni are increased (32 and 35 at.%), while the content of Cr is decreased (20 at.%). The addition of 3 at.% Mo is to prevent the coarsening of the L₁₂ nanoprecipitates, and also to enhance the effect of solid solution strengthening. The raw materials were melted in a vacuum induction furnace protected by argon gas. The alloy ingot with size of 112 × 100 × 100 mm³ was homogenized at 1200 °C for 36 h and then hot rolled to 20 mm followed by water cooling. After removal of surface oxides, the sheet was further cold rolled to 11.5 mm. In order to obtain uniform equiaxed grains, the sheet was water cooled after solid solution at 1200 °C for 4 min. In order to obtain nanoprecipitates, the solid solution MEA was aged at 650 °C for 30 h. The 500 μm thick slices were cut in solid solution and aging MEAs by electric discharge machining. The sheets were ground on both sides using 3000# SiC paper, and then mechanically and electrolytically polished to 200 μm thickness (samples in solid solution and aging states were labeled as SS and AG, respectively).

The irradiation experiment was performed at Lanzhou Institute of Modern Physics using 3 MeV Fe¹¹⁺ ions at 500 °C. The atomic displacement threshold energy of Cr, Fe, Ni, Nb, Mo and Al are 40 eV, 40 eV, 40 eV, 40 eV, 60 eV and 27 eV, respectively [56]. The surface binding energy of Cr, Fe, Ni, Nb, Mo and Al are 3.27 eV, 2.32 eV, 3.74 eV, 5.93 eV, 5.32 eV and 3.19 eV, respectively [57]. The damage profile was calculated using SRIM-2013 in the Kinchin-Pease mode [58]. The damage depth was ~ 843 nm to the surface with the peak damage level of ~ 58 displacement per atom (dpa) as show in Fig. 1. The fluence was 5.45×10^{16} ion/cm². The irradiation process lasted for 40 h at 500 ± 10 °C. The vacuum of the irradiation chamber was $\sim 5 \times 10^{-5}$ Pa. The samples after irradiation were labeled as SSIR and AGIR, respectively. According to the prediction of damage depth of SRIM (Fig. 1), the depth range can be divided into three regions: Region I (0 ~ 500 nm), Region II (500 ~ 1344 nm), and Region III (above 1344 nm). Region I (0 ~ 500 nm) and Region II (500 ~ 1344 nm) are irradiated regions, while Region III (above 1344 nm) is unirradiated region.

Transmission electron microscope (FEI Talos F200) was used to identify the microstructure after radiation damage of the matrix and nanoprecipitates. SS and AG specimens were mechanically thinned to

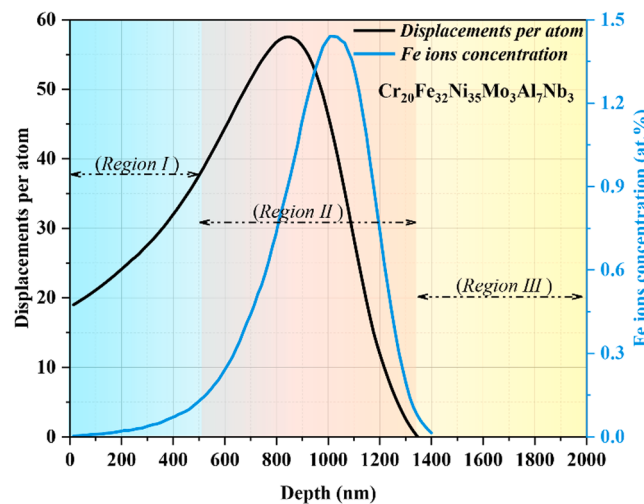


Fig. 1. Depth profiles of dpa and injected interstitial profile predicted by SRIM for $\text{Cr}_{20}\text{Fe}_{32}\text{Ni}_{35}\text{Mo}_3\text{Al}_7\text{Nb}_3$ MEA irradiated with 3 MeV Fe^{11+} ions at a fluence of 5.45×10^{16} ions/ cm^2 .

about 40 μm , punched into $\Phi 3$ mm circle sheets, and then thinned by ion beam milling. Cross-sectional TEM specimens of the SSIR and AGIR alloys along the depth direction from the irradiated surface were prepared

by focused ion beam (FIB) method using the conventional lift-out technique. The thickness of TEM samples was measured to be ~ 100 nm by convergent-beam electron diffraction (CBED) in both the SSIR and AGIR samples. Nanoindentation tests were performed before and after irradiation (G200 nanoindenter instrument, Agilent). A Berkovich-type indenter with 20 nm size was used to obtain the relationship between indentation depth and hardness using the continuous stiffness measurement (CSM) method. The average hardness of each sample was calculated from ten indentation tests to avoid statistical errors.

3. Results

3.1. Microstructures evolutions in SSIR and AGIR samples

Fig. 2 is used to show the microstructure evolutions before and after irradiation, in order to study the SSIR and AGIR samples after irradiation, including possible precipitation and dissolution. In **Fig. 2a**, the bright field (BF) and the selective electron diffraction patterns (SAED) images on [110] zone axis confirm that the matrix of the solid-solution sample is FCC structure. Due to the absence of superlattice diffraction spots of L1_2 nanoprecipitates, the dark field (DF) imaging of L1_2 nanoprecipitates cannot be performed. In addition, the FCC structure in the matrix of the solid-solution sample is consistent with that of SSIR-Region III (**Fig. 2e** and **e**₃). At least 200 nanoprecipitates were involved in determining the equivalent average radius of nanoprecipitates for AG sample. The representative images are shown in **Fig. 2(b-d)**, the average

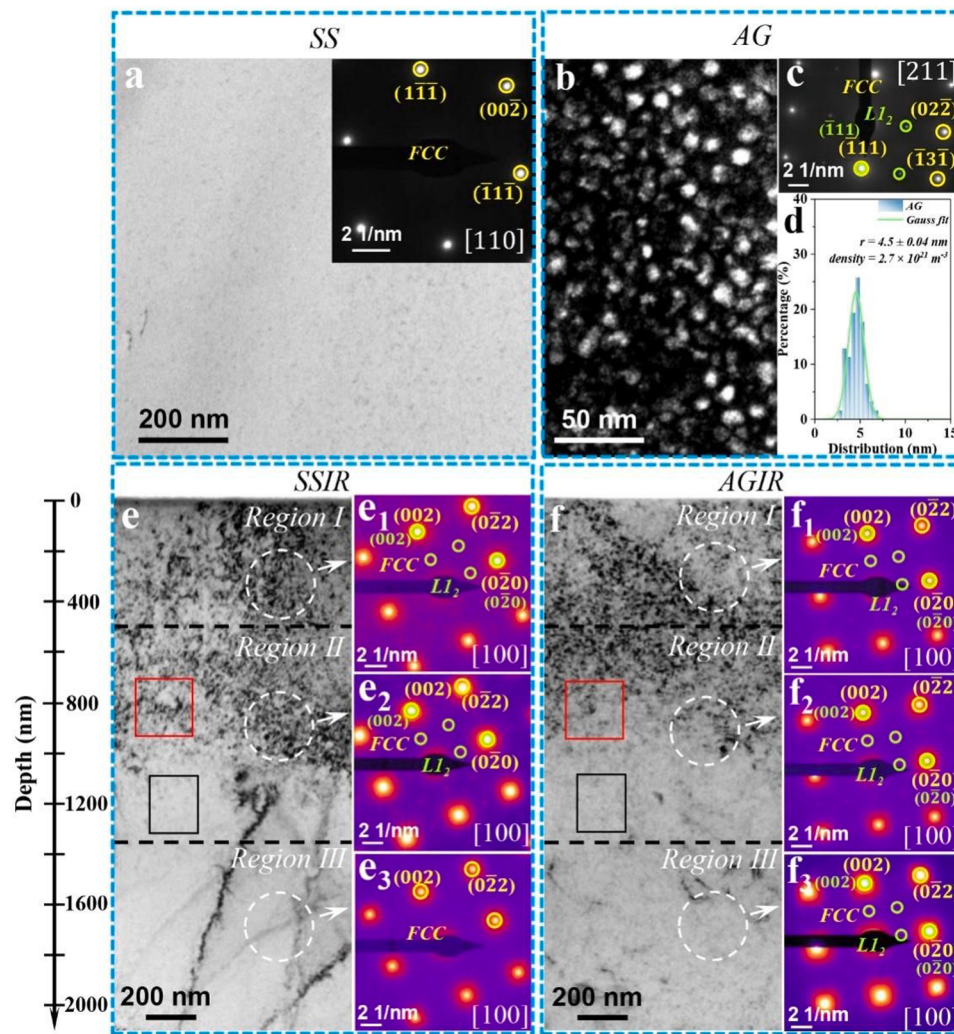


Fig. 2. Microstructure of the SS and AG samples and irradiation damage cross sections of the SSIR and AGIR samples: (a) The microstructure of the SS sample and the diffraction spots; (b-c) The central DF image of L1_2 nanoprecipitates and the diffraction spots in the AG sample; (d) The distribution of nanoprecipitates of the AG sample; (e) SSIR irradiation damage section; (e₁-e₃) The diffraction spots in the Region I, Region II and Region III reveal the FCC matrix and/or L1_2 ordered structure of the SSIR sample; (f) AGIR irradiation damage section; (f₁-f₃) The diffraction spots in the Region I, Region II and Region III reveal the FCC matrix and L1_2 ordered structure of the AGIR sample.

equivalent average radius (r) was calculated according to the following equations [60,61]:

$$r_p = \sqrt{A_p/\pi} \quad (1)$$

$$r = \frac{1}{n} \sum_{i=1}^n r_p^i \quad (2)$$

In the aging sample the average equivalent radius of the preexisting L₁₂ nan precipitates is $\sim 4.5 \pm 0.04$ nm and the number density is 2.7×10^{21} m⁻³, which is consistent with AGIR-Region III with diffraction spots of L₁₂ nan precipitates (Fig. 2f and f₃). It is demonstrated that although SSIR-Region III was not irradiated, annealing at 500 °C (irradiation temperature) for 40 h did not induce the precipitation in the SSIR-Region III. The cross sectional microstructures are shown in Fig. 2 (e-f₃). Fig. 2e shows the BF from the surface to the depth of 2000 nm of the SSIR sample. In Fig. 2(e₁-e₃), a series of SAEDs were obtained from three regions of Region I, Region II and Region III along the [100] axis in Fig. 2e. The results show that the superlattice diffraction spots of the L₁₂ ordered structure appeared in both Region I and Region II. It was confirmed that Fe¹¹⁺ ion irradiation induced the precipitation of ordered L₁₂ phase in the SSIR-Region I and SSIR-Region II, while there was no precipitation in the SSIR-Region III. The precipitation temperature of the ordered L₁₂ phase is usually below 600 °C [59]. Therefore, 500 °C annealing did not lead to the precipitation of the ordered L₁₂ phase in the unirradiated region III.

Fig. 2f shows the BF image from the surface to the depth of 2000 nm of the AGIR sample. In Fig. 2(f₁-f₃), a series of SAED images were obtained from three regions of the AGIR-Region I, Region II and Region III in Fig. 2f along the [100] axis. These results show that there were still superlattice diffraction spots of the L₁₂ ordered structure in all the three regions. The red and black frames in Fig. 2e and f correspond to the peak damage region at ~ 843 nm and the damage region at ~ 1200 nm, respectively. STEM/ two-beam BF images are further conducted to show

the dislocation/loops in Fig. 7.

In Fig. 3, the central DF image further shows the morphology and the equivalent average radius distribution of the L₁₂ precipitates. The DF image obtained from the superlattice diffraction spots of the L₁₂ precipitates directly shows its distribution in each region. The size of L₁₂ nanoprecipitates was estimated according to the method of equivalent circle radius by Eqs. (1-2). As shown in Fig. 3(a₁-a₂), the shape of L₁₂ nanoprecipitates in the SSIR-Region I was irregular. The equivalent average radius was $\sim 1.3 \pm 0.04$ nm with number density of $\sim 6.5 \times 10^{22}$ m⁻³. The L₁₂ nanoprecipitates in the SSIR-Region II were still irregular with an equivalent average radius of $\sim 2.7 \pm 0.05$ nm, and the number density decreased to $\sim 5.1 \times 10^{21}$ m⁻³ (Fig. 3b₁-b₂). In the SSIR sample, annealing at 500 °C cannot induce the precipitation of L₁₂ nanoprecipitates, indicating that ion irradiation is the key factor to induce the precipitation. In particular, as shown in Fig. 3a₂ and b₂, L₁₂ nanoprecipitates show different precipitation trends in Region I and Region II of the SSIR sample. Although the equivalent average radius of the L₁₂ nanoprecipitates in the SSIR-Region II only increased by ~ 1.4 nm, the size distribution range of the L₁₂ nanoprecipitates in the SSIR-Region II was significantly wider than that of the SSIR-Region I with a maximum radius of ~ 9 nm, which had a more concentrated equivalent radius distribution. Therefore, in addition to the dominant role of irradiation enhanced diffusion in the evolution of L₁₂ nanoprecipitates in the SSIR sample, it should not be ignored that a high dose is more conducive to promoting the growth of nanoprecipitates.

Fig. 3(c₁-c₂), (d₁-d₂) and (e₁-e₂) reveal the characteristics of the L₁₂ nanoprecipitates in the Region I, Region II and Region III of the AGIR sample. Different from the aging MEA [45], the nanoprecipitates in the AGIR-Region I and AGIR-Region II changed from spherical to irregular shape. Fig. 2(c₁-c₂) show the DF images of the L₁₂ nanoprecipitates in the AGIR-Region I, and the shape of the L₁₂ nanoprecipitates become irregular. In addition, the equivalent average radius of the L₁₂ nanoprecipitates in the AGIR-Region I is $\sim 3.8 \pm 0.05$ nm, and the number density is $\sim 2.3 \times 10^{21}$ m⁻³. As the peak dose increased to ~ 58 dpa

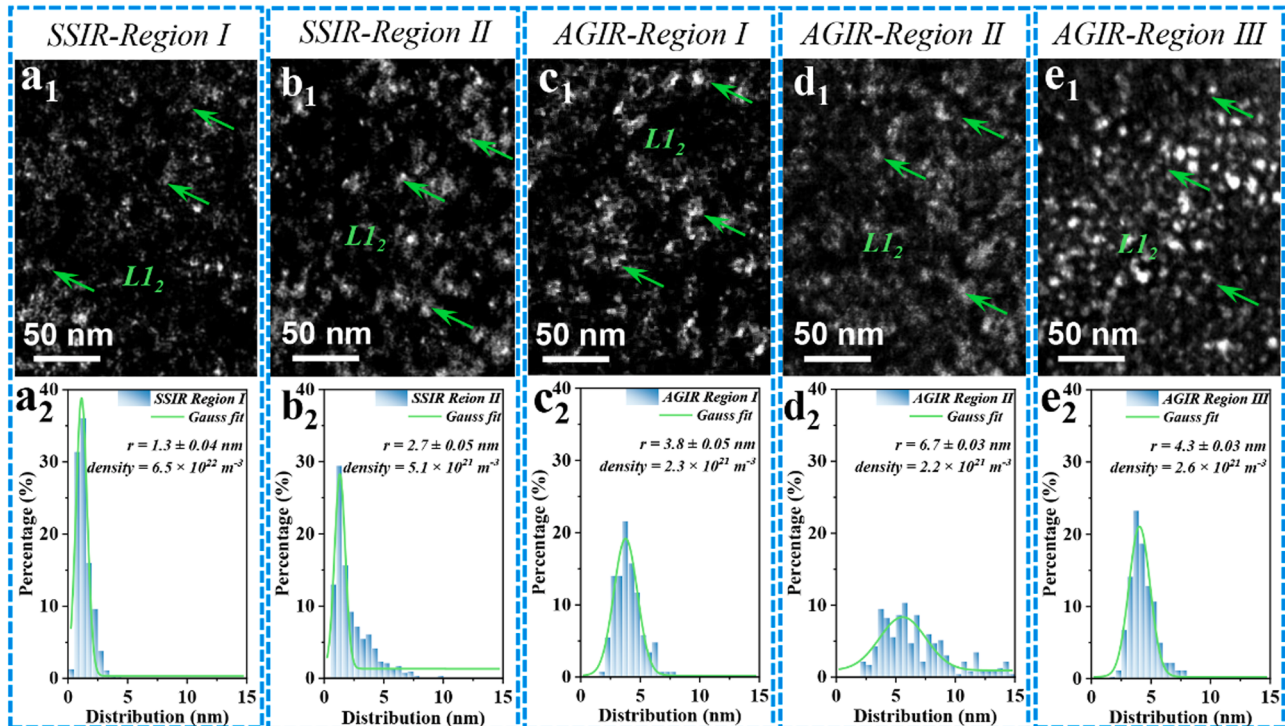


Fig. 3. The evolutions of nanoprecipitates in the SSIR and AGIR samples vary with depth: (a₁-a₂) DF image and distribution of nanoprecipitates in the Region I of the SSIR sample; (b₁-b₂) DF image and distribution of nanoprecipitates in the Region II of the SSIR sample; (c₁-c₂) DF image and distribution of nanoprecipitates in the Region I of the AGIR sample; (d₁-d₂) DF image and distribution of nanoprecipitates in the Region II of the AGIR sample; (e₁-e₂) DF and distribution of nanoprecipitates in the Region III of the AGIR sample.

(AGIR-Region II), the interface between the matrix and L₁₂ nanoprecipitates became quite rough (Fig. 2d₁). Furthermore, the L₁₂ nanoprecipitates even lost spherical characteristics. The equivalent average radius of the nanoprecipitates was $\sim 6.7 \pm 0.03$ nm with number density of $\sim 2.2 \times 10^{21} \text{ m}^{-3}$. The nanoprecipitates in the Region III was still spherical with an average radius of $\sim 4.3 \pm 0.03$ nm and number density of $\sim 2.6 \times 10^{21} \text{ m}^{-3}$. The shape and average radius of the nanoprecipitates were not affected by thermal annealing at 500 °C. As shown in Fig. 3(e₁-e₂), the L₁₂ nanoprecipitates in the AGIR-Region

III maintained excellent stability with an average radius of $\sim 4.3 \pm 0.03$ nm. Therefore, it can be concluded that the evolutions of the L₁₂ nanoprecipitates in the AGIR-Region I and Region II were caused by irradiation, and the nanoprecipitates in AGIR-Region III is similar to that in AG sample with no change. It is demonstrated that although SSIR-Region III and AGIR-Region III were not irradiated, annealing at 500 °C (irradiation temperature) for 40 h did not induce the precipitation in the SSIR-Region III or the dissolution or coarsening of nanoprecipitates in the AGIR-Region III. Since the irradiation depth is only

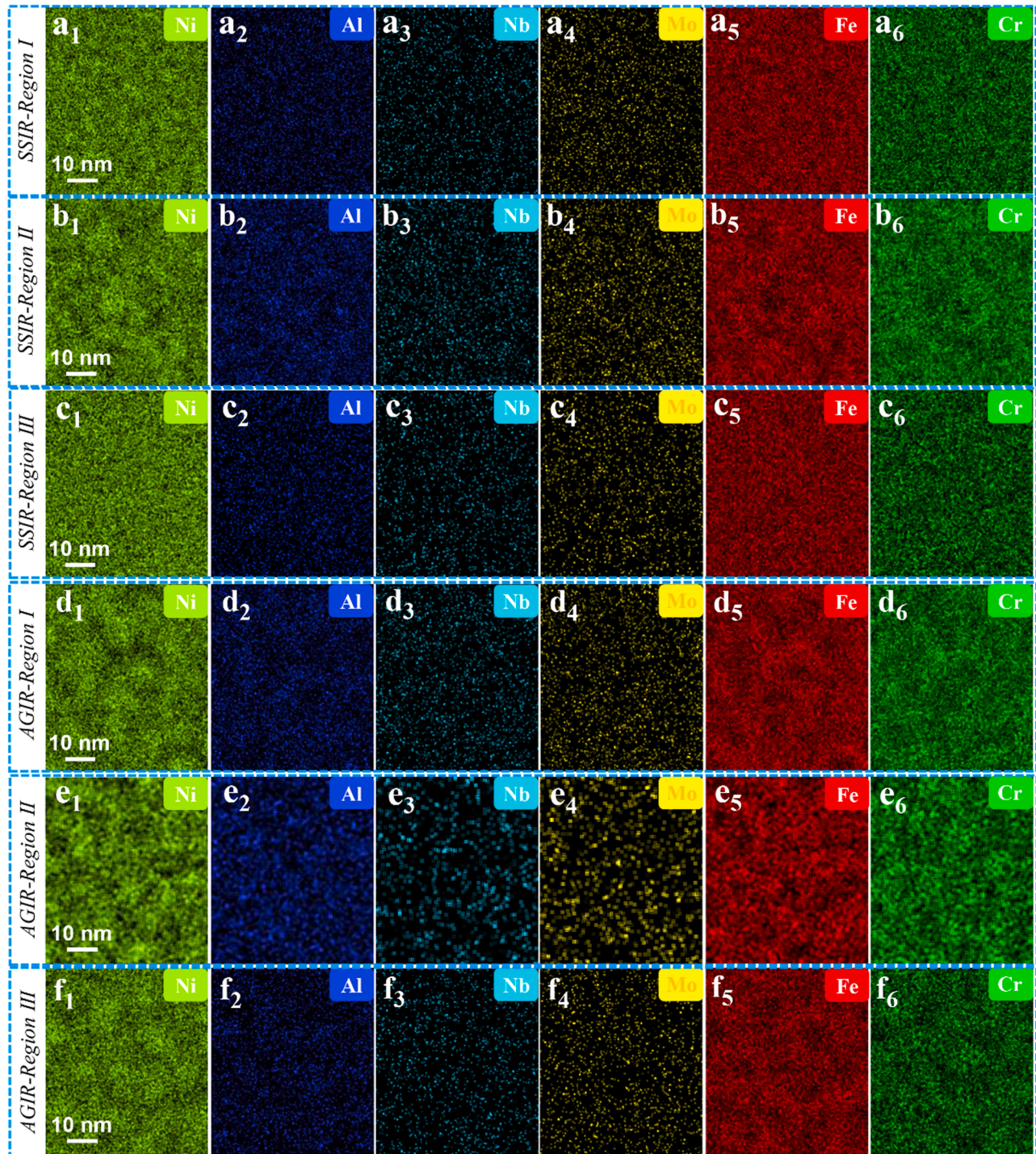


Fig. 4. The composition of nanoprecipitates in the SSIR and AGIR samples varies with irradiation depth. (a₁-a₆) EDS-mappings of the SSIR-Region I, (b₁-b₆) EDS-mappings of the SSIR-Region II, (c₁-c₆) EDS-mappings of the SSIR-Region III, (d₁-d₆) EDS-mappings of the AGIR-Region I, (e₁-e₆) EDS-mappings of the AGIR-Region II, (f₁-f₆) EDS-mappings of the AGIR-Region III.

~1344 nm, Region III (~1344 nm from the surface) is not affected by irradiation. Thus, Region III is considered as un-irradiated region. The microstructures of Region III in both SSIR and AGIR samples are treated as the initial microstructure prior to irradiation.

Fig. 4(a₁–a₆), (b₁–b₆) and (c₁–c₆) show the EDS mappings of the SSIR-Region I, SSIR-Region II and SSIR-Region III, respectively. The results showed that L1₂ Ni-Al precipitates with irregular shapes appeared in the SSIR-Region I and Region II. However, the interface between the Ni-Al precipitate and matrix gradually becomes prominent with increasing irradiation dose. The enrichment degree of Al is significantly less than that of Ni with the ratio of Ni and Al elements of approximately 3:1. Fig. 4(d₁–d₆), (e₁–e₆), and (f₁–f₆) show the EDS mappings of the AGIR-Region I, Region II, and Region III, respectively. The interface of the nanoprecipitates in the AGIR-Region I is no longer clear but become somewhat fuzzy, indicating the occurrence of early dissolution. Interestingly, the enrichment of Ni and Al within the nanoprecipitates is still obvious, but the interface of nanoprecipitates cannot be clearly distinguished in the EDS-mapping image, which is consistent with the phenomenon observed by Cao et al. [43]. With the increase of doses (from ~24 to ~58 dpa), the interfaces between the matrix and nanoprecipitates become pretty rough in the AGIR-Region II, and the shape of nanoprecipitates is no longer spherical. In the AGIR-Region III (identified as the un-irradiated region), Ni and Al maintain spherical enrichment, and Fe and Cr show spherical depleted with obvious interfaces (Fig. 4f₁–f₆). In the un-irradiated Region III, the nanoprecipitates retained original shape.

3.2. Radiation-induced voids and swelling

Fig. 5a shows the TEM image of the under-focused BF cross section of the SSIR alloy. A small number of voids appear in the depth range of 1100 ~ 1377 nm far away from the damage peak, which is consistent with the results of Lu et al. [21]. The voids are marked in the region of the pink dotted line. Figs. 5(b–c) show the enlarged BF view in the under-focused and over-focused images of the voids. In the range of 1100 ~ 1377 nm, it is found that a small amount of voids are captured by L1₂ nanoprecipitates induced by irradiation in the Region II, as shown in Fig. 5(d–e). Fig. 5(f–g) show the BF under-focused cross section of the AGIR sample and the enlarged images of the corresponding position. No voids are found in the cross section and enlarged image. Both under-focused and over-focused BF images in the depth range of 1100 ~ 1377 nm shown in Fig. 5(g–h) indicate the absence of voids in the AGIR sample. In order to investigate the swelling resistance, the swelling rate of the SSIR and AGIR alloys can be estimated by Eq. (3) [22]:

$$S(\%) = \frac{\frac{\pi}{6} \sum_{i=1}^N d_i^3}{A \times \delta - \frac{\pi}{6} \sum_{i=1}^N d_i^3} \times 100 \quad (3)$$

Where S represents the swelling rate, d_i is the diameter of each void, A is the area containing the voids from the surface to the depth of ~1344 nm. δ is the thickness of the TEM sample in this area (~100 nm). The swelling of the SSIR alloy is calculated to be $5.5 \times 10^{-4}\%$ with a swelling rate of $9.4 \times 10^{-6}\%/\text{dpa}$, while the AGIR alloy has no swelling.

3.3. Mechanical properties

Hardness can be used to reflect the mechanical properties variations caused by radiation. Fig. 6 shows the comparison of hardness of the SS, SSIR, AG and AGIR samples. As the hardness value of nanoindentation at a certain depth generally reflects the real hardness of 3–5 times of depth, the hardness at ~260 nm (0.31 times of the damage peak depth) is selected to represent the hardness at the damage peak. After ion irradiation, the hardness of the SSIR sample increases from ~3.60 to ~5.58 GPa, showing obvious irradiation hardening, which is related to the precipitation of L1₂ nanoprecipitates and the evolution of defects such as voids. Compared with the SS sample, the hardness increment of the AG sample is ~1.92 GPa. The hardness of the AG sample is similar to that of the SSIR sample. The hardness of the AGIR sample keeps almost

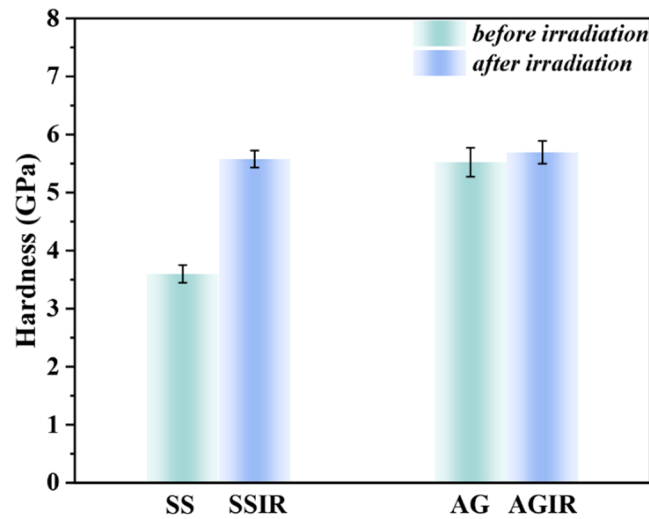


Fig. 6. Hardness comparisons of the SS, SSIR, AG and AGIR samples.

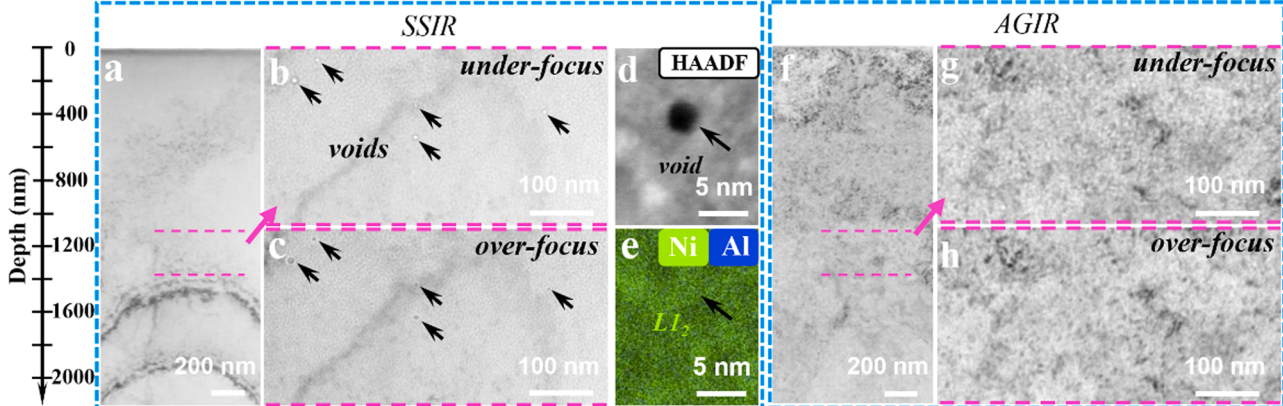


Fig. 5. Cross-sectional TEM images of the SSIR and AGIR samples. (a) The cross-sectional TEM BF image of the SSIR sample. (b–c) are the representative enlarged images of voids in the under-focused and over-focused images in the SSIR sample, respectively. (d–e) show evidence of voids trapped by nanoprecipitates in the SSIR-Region II, respectively. (f) The cross-sectional TEM BF image of the AGIR sample. (g–h) are the representative enlarged images in the under-focused and over-focused images of the AGIR-region II, where no voids can be found.

unchanged compared with the AG sample, indicating that irradiation does not cause hardening. By comparison, the preexisting L1₂ nanoprecipitates can mitigate the irradiation hardening effect.

4. Discussion

4.1. Radiation-induced precipitation and coarsening mechanisms in the SSIR and AGIR samples

The evolution of nanoprecipitates during irradiation is driven by two competing processes: one is the reordering process driven by irradiation enhanced diffusion, which can help growth, coarsening or reprecipitation of nanoprecipitates; the other is the contraction or even dissolution of the nanoprecipitates caused by the ballistic dissolution, which eventually leads to the decrease of the diameter and number density [42,43, 62,63]. These are two opposite ways of qualitatively affecting nanoprecipitates formation and stability, i.e. the competition between these two effects provides a steady-state situation for the nanoprecipitates that is not in thermal equilibrium, guiding the nanoprecipitates to an optimum size [63]. It is also reported that irradiation causes carbide to grow or shrink depending on whether the size is less than or greater than the optimum size in 316 stainless steel [63].

The evolution law of nanoprecipitates in the SSIR sample has been analyzed in Section 3.1, that is, the equivalent radius increases and the number density decreases with the increase of irradiation dose (Fig. 3a₂ and b₂), which confirms the correlation between the growth of nanoprecipitates and irradiation dose. Since irradiation induced precipitation [64] and aging induced precipitation are both diffusion controlled [65–67], the effect of irradiation dose on precipitation is discussed according to the irradiation enhanced diffusion mechanism [36,64]. The irradiation enhanced diffusion coefficient (D') under steady state is shown in Eq. (4) [64]:

$$D' = \frac{2K}{k_v^2} + D_v \quad (4)$$

Where D_v is the vacancy self-diffusion coefficient without irradiation (thermal diffusion coefficient), K is the damage rate. The average damage rate of the SSIR-Region I and AGIR-Region I was $\sim 1.7 \times 10^{-4}$ dpa/s, while that of the SSIR-Region II and AGIR-Region II was $\sim 4.0 \times 10^{-4}$ dpa/s. k_v^2 is the sink strength for interstitials or vacancies (equal sink strengths are assumed). The sink strength for nanoprecipitates can be written as [64]:

$$k_v^2 = k_p^2 = 4\pi r\rho Y \quad (5)$$

Where r and ρ are radius and number density of the coherent nanoprecipitates, and Y relates to the bias for defect trapping, assuming $Y \approx 1$ [64]. According to the evaluation of Eqs. (4) and (5), the contributions of irradiation to D' are 3.2×10^{-19} m²/s and 4.6×10^{-18} m²/s in the SSIR-Region I and SSIR-Region II, respectively. Al content controlled the formation of L1₂ nanoprecipitates during hot aging process [65,66]. Therefore, in the case of thermal diffusion, the diffusion coefficient (D_v) of Al is calculated according to the Arrhenius diffusion coefficient equation, as shown in Eq. (6) [68]:

$$D_v = D_0 \exp\left(\frac{-Q}{RT}\right) \quad (6)$$

Where D_0 is the pre-exponential factor (1.0×10^{-4} m²/s) and Q is the activation energy of the diffusion (276 kJ/mol) [68–70]. R is the gas constant (8.31 J/mol·K) [68], and T is the absolute temperature (773.15 K). The diffusion coefficient of Al in pure Ni at 500 °C is calculated to be 2.2×10^{-23} m²/s. Therefore, it can be calculated that diffusion in the SSIR sample is enhanced by irradiation by more than 10^4 times (1.5×10^4 times in the SSIR-Region I and 2.1×10^5 times in the SSIR-Region II).

However, the nanoprecipitates in the AGIR-Region I and AGIR-

Region II after irradiation showed different evolution phenomena, that is, the nanoprecipitates tended to shrink in the AGIR-Region I, while the nanoprecipitates tended to coarsen or even reprecipitate in the AGIR-Region II (Fig. 3c₂ and d₂). Interestingly, there are no other factors affecting the evolution of nanoprecipitates except the difference irradiation dose in these two irradiated regions. Therefore, it is reasonable to determine the evolution of nanoprecipitates dominated by the ballistic dissolution mechanism in the AGIR-Region I and the mixed mechanism of irradiation enhanced diffusion and ballistic dissolution in the AGIR-Region II, respectively. Here, the ballistic dissolution mechanism and the mixing mechanism are discussed respectively according to the influence of irradiation dose on the evolution of nanoprecipitates. In addition, Du et al. [42,43] found that irradiation precipitation, coarsening and even dissolution of L1₂ or B₂ nanoprecipitates are controlled by the diffusion of Al element. The fastest diffusion rate of Al and ordered superlattice structure control the precipitation process, and the relatively small atomic mass of Al allows it to be displaced for a longer distance after ballistic collision with ions [42,43,71]. Therefore, the evolution of nanoprecipitates in each irradiated region is controlled by Al. To understand the complexity, the Ostwald coarsening model of Lescoat et al. [72] is applied here to determine the relative possibilities of shrinkage due to ballistic dissolution and coarsening or even reprecipitation due to mixing mechanisms. Ballistic dissolution coefficient (D^B) is shown in Eq. (7):

$$D^B = \frac{1}{6}K\langle\bar{x}^2\rangle \quad (7)$$

Where K is the damage rate. \bar{x} is the average distance of the atomic motion of Al caused by the cascade collision. Here, the difference of equivalent diameter between the AGIR-Region III and AGIR-region I or AGIR-region II is used instead \bar{x} . Hence, Al atomic motion distance due to collision cascade within the average distance (\bar{x}) were estimated to be ~ 1.0 nm and 4.8 nm in the AGIR-Region I and AGIR-Region II, respectively. According to Eq. (7), the ballistic solubility coefficient in the AGIR-Region I is 2.8×10^{-23} m²/s. Therefore, the diffusion coefficient controlled by irradiation enhanced diffusion and thermal diffusion in the AGIR-Region II is 4.3×10^{-18} m²/s according to Eq. (4), which is much higher than the ballistic dissolution coefficient of 1.5×10^{-21} m²/s according to Eq. (7), indicating that the nanoprecipitates tends to coarsen or even reprecipitate.

4.2. Irradiation-induced hardness change mechanisms in the SSIR and AGIR samples

It is well known that defect structures induced by irradiation, such as dislocation loops, voids and nanoprecipitates, lead to mechanical properties changes that harden or soften the materials [73,74]. In this study, the L1₂ nanoprecipitates, dislocation loops and voids are considered to be the main factors that affect the yield strength of the irradiated MEAs. The dispersed barrier hardening (DBH) model [75] can be used to calculate the change in yield strength ($\Delta\sigma_i$), which is given by Eq. (8):

$$\Delta\sigma_i = \alpha_i M G b \sqrt{\rho_i d_i} \quad (8)$$

Where, α_i is the defect strength factor, depending on the type of defects [75]. M is the Taylor factor (3.06 for FCC alloys), G is shear modulus (80 GPa [45,76]), b is the magnitude of the Burgers vector (0.253 nm), ρ_i and d_i are the number density and average size of the defect, and i represents the type of irradiation defect. In particular, the high dependence of DBH model on α_i increases the difficulty in evaluating mechanical properties [5,77,78]. Therefore, it is necessary to use the modified formula developed by Chen et al. [78,79] to analyze the intensity factor α_i with different types of defects. The following modified models are used to calculate the intensity factor of L1₂ nanoprecipitates and voids, respectively [78,79]:

$$\alpha_{L1_2} = \frac{0.816\gamma d}{Gb^2(1 - 0.816d\sqrt{\rho_{L1_2}d})} + 1.7\left(\frac{d}{b}\right)^{1.5}\epsilon^{1.5} + 0.0054\left(\frac{d}{b}\right)^{0.275}\left(\frac{\Delta G}{G}\right)^{1.5} \quad (9)$$

$$\alpha_{voids} = k_1 \ln(k_2 d) \quad (10)$$

Where γ is the interfacial energy of the matrix and $L1_2$ nanoprecipitates (0.102 J/m^2 [78]), ΔG is the double-phase shear modulus mismatch ($\Delta G = G_{FCC} - G_{L1_2} = 3 \text{ GPa}$ [59]), ϵ is the double-phase lattice mismatch ($\epsilon = 0.002$), k_1 and k_2 are respectively 0.4654 and 0.9378 for the experimental fitting parameters of α_{voids} [78,79]. Then α_{L1_2} and α_{voids} in the SSIR sample are calculated to be 0.1 and 0.7, respectively. In the AGIR sample, α_{L1_2} is 0.29, while $\alpha_{voids} = 0$. In addition, the irradiation induced dislocation loops lead to the increase of yield strength, which can be described using Bailey-Hirsch equation [59,80]:

$$\Delta\sigma_{loop} = \beta MGbp^{1/2} \quad (11)$$

Where $\beta = 0.2$ is the constant for FCC metal [59], ρ stands for the dislocation density. Fig. 7 illustrates the STEM-BF images and two-beam BF sub-images from [001] zone axis, showing the microstructure of the dislocation/loops within the damage peak range at $\sim 843 \text{ nm}$ (Fig. 7a₁-a₂ and b₁-b₂) and the damage region at $\sim 1200 \text{ nm}$ of the SSIR and AGIR samples (Fig. 7a₃ and b₃). The corresponding damage at $\sim 1200 \text{ nm}$ depth is $\sim 10 \text{ dpa}$ from the SRIM calculation. The average size of dislocation loops in the SSIR sample is $8.9 \pm 0.09 \text{ nm}$ with number density of $6.4 \times 10^{13} \text{ m}^{-2}$ (Fig. 7a₂) in the damage peak range. However, the average size and number density in the AGIR sample decreased by $\sim 40\%$ and $\sim 28\%$ compared with the SSIR sample (Fig. 7b₂) in the damage peak range, respectively. In the SSIR MEA, the yield strength increase caused by irradiation induced precipitation, voids and dislocation loops are 33 MPa, 25 MPa and 99 MPa,

respectively. In the AGIR MEA, the yield strength increases by 98 and 84 MPa due to the $L1_2$ phases precipitation and dislocation loops formation, respectively. In addition, Foreman and Makin's model [81] was used to estimate the overall contribution of different kinds of defect structures on the changes of mechanical properties ($\Delta\sigma_{total}$) after radiation. Since the AGIR alloy did not contain voids, the influence of voids was not considered. The $\Delta\sigma_{total}$ value can be obtained from Eq. (12) [81]:

$$\Delta\sigma_{total} = \sqrt{(\Delta\sigma_{L1_2})^2 + (\Delta\sigma_{loop})^2 + (\Delta\sigma_{void})^2} \quad (12)$$

Where, $\Delta\sigma_{L1_2}$, $\Delta\sigma_{loop}$ and $\Delta\sigma_{void}$ are the mechanical properties changes caused by each kind of irradiation defect respectively, i.e., each term $\Delta\sigma_i$ in Eq. (8). According to Eq. (12), compared with the SS sample, the irradiation hardening increment in the SSIR and AGIR samples are 107 MPa and 129 MPa, respectively. The strength factor (α_{L1_2}) of the nanoprecipitates in the AG sample is 0.17, and the $\Delta\sigma_{total}$ of the AG sample is 50 MPa. Therefore, it can be seen that the yield strength of the AG alloy increases by 79 MPa after irradiation. In the SSIR sample, $L1_2$ nanoprecipitates, voids, and loops contributed to the hardness increment of 33 MPa, 25 MPa and 99 MPa, respectively. The contribution of loops to hardness (84 MPa) in the AGIR sample is basically the same as that in the SSIR sample (99 MPa). In contrast, the elimination of voids and the reprecipitation of $L1_2$ nanoprecipitates make the hardness of the AGIR sample remain almost unchanged.

4.3. Swelling in the SSIR and AGIR samples

Studies have shown that the fundamental reason why HEA/MEAs possess good irradiation tolerance is that the complexity of components inhibits the evolution of defects, significantly reducing the swelling [4, 15,25]. However, increasing the complexity of components inevitably leads to a higher proportion of Frank dislocation loops in irradiated

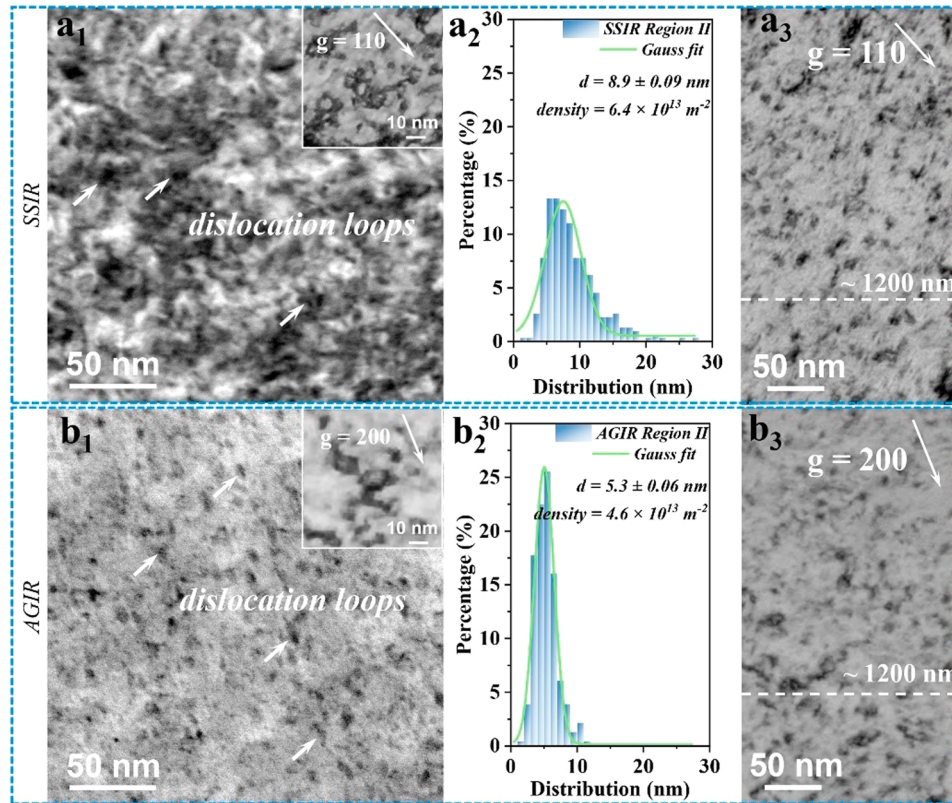


Fig. 7. STEM-BF and two-beam condition BF images of dislocation loops. (a₁-a₂) The dislocation loops and its distribution in SSIR sample within the damage peak region; (a₃) two-beam condition BF images of dislocation loops within the $\sim 1200 \text{ nm}$ in SSIR sample; (b₁-b₂) The dislocation loops and its distribution AGIR sample within the damage peak region; (b₃) two-beam condition BF images of dislocation loops within the $\sim 1200 \text{ nm}$ in AGIR sample.

alloys and leads to irradiation hardening [4,15,16,19,21]. In this study, the components of the SSIR and AGIR alloys were consistent, ruling out the effect of component complexity. Compared to most HEAs/steels [4, 21,27,82–101], the SSIR alloy shows the lowest swelling rate ($9.4 \times 10^{-6} \text{ %/dpa}$) after irradiation of $\sim 58 \text{ dpa}$ at 500°C (Fig. 8). Furthermore, the AGIR sample presents a better irradiation resistance without swelling under the same irradiation condition.

As discussed in Section 4.1, in the SSIR sample, the precipitation of L_1_2 nanoprecipitates is promoted by irradiation. The equivalent radius is positively correlated with the damage rate. In the AGIR sample, nanoprecipitates contracted in the AGIR-region I (Fig. 3c₁), coarsened and reprecipitated in the AGIR-region II (Fig. 3d₁). It can be inferred that the dissolution of nanoprecipitates occurred under irradiation, but reprecipitation also occurred in the enrichment region of nanoprecipitate forming elements. This frequent reprecipitation appeared to be responsible for the maintenance of the high-number-density nanoprecipitates [42]. Obviously, based on the minimal lattice mismatch between FCC matrix and L_1_2 nanoprecipitates ($\epsilon \sim 0.002$ in this work), the easier the dissolution of nanoprecipitates is, the easier it is to promote reprecipitation, which is more conducive to the dynamic disordered transformation of nanoprecipitates, effectively eliminating the defects generated by irradiation [42]. Despite of high-dose radiation, the irradiation defects involved in this recombination process are largely eliminated. As shown in Fig. 5(d–e), in the SSIR sample, the voids are captured by L_1_2 nanoprecipitates induced by irradiation. STEM-BF images of the SSIR and AGIR samples in the damage peak region further confirm the precipitation and dissolution of nanoprecipitates, effectively reducing the diameter of dislocation loops from $8.9 \pm 0.09 \text{ nm}$ to $5.3 \pm 0.06 \text{ nm}$ and the number density from $6.4 \times 10^{13} \text{ m}^{-2}$ to $4.6 \times 10^{13} \text{ m}^{-2}$ (Fig. 7). When irradiation guides the nanoprecipitates to the optimal size, irradiation may also lead to the contraction or even re-precipitation of nanoprecipitates. The AGIR sample also follows this process. The similarity of these two ways to induce nanoprecipitates precipitation has been well proved by previous studies [73,74]. Therefore, in the SSIR or AGIR samples, with the extension of irradiation time, the voids are captured, and the voids or dislocation loops even recombine by the precipitation and dissolution of L_1_2 nanoprecipitates. In addition, the low mismatch between L_1_2 nanoprecipitates and FCC MEA matrix and the low interfacial energy (0.102 J/m^2 [78]) greatly shorten the incubation time and reduce the nanoprecipitates nucleation barrier, which is conducive to the reshuffle process during the evolution of nanoprecipitates and eliminate the voids or the dislocation loops. In particular, the co-precipitation of nanoprecipitates and voids in the SSIR-Region II during irradiation and their trapping relationship can fully prove that the voids are still the preferred locations for re-precipitation of nanoprecipitates. Through this relationship and precipitation and dissolution of nanoprecipitates, the high density nanoprecipitates ($\sim 10^{21} \text{ m}^{-3}$) are dynamically retained, the swelling rate is effectively controlled.

5. Conclusions

In summary, this paper reports the enhancement of irradiation tolerance of cobalt-free MEA under high-temperature and high-dose irradiation by precipitation and dissolution of nanoprecipitates. The following conclusions can be drawn:

- (1) The evolution of nanoprecipitates in the SSIR sample was driven by the irradiation enhanced diffusion mechanism. The equivalent radius increased and number density decreased with the increase of diffusion coefficient. While the evolution of nanoprecipitates in the AGIR-region I and AGIR-region II were driven by the ballistic dissolution mechanism and mixing mechanism, respectively. The nanoprecipitates tended to shrink in the AGIR-region I, while the nanoprecipitates tended to coarsen or even reprecipitate in the AGIR-region II.

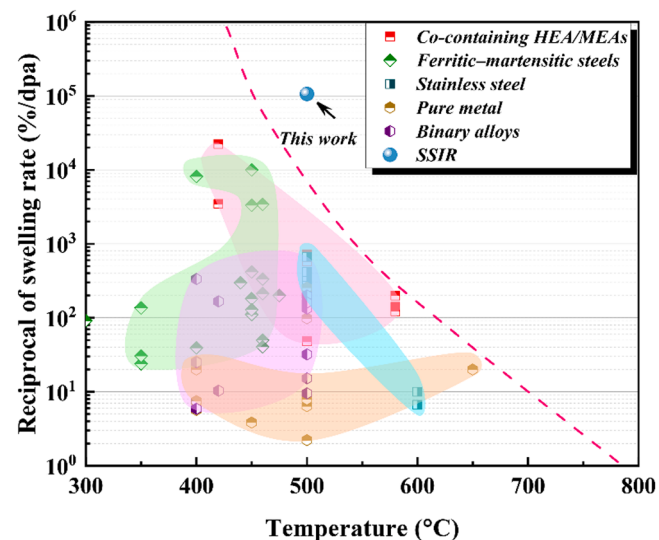


Fig. 8. Ashby map of temperature versus the reciprocal swelling rate in various alloy systems.

- (2) After irradiation, the SSIR sample occurred irradiation hardening owing to the precipitation of L_1_2 nanoprecipitates, dislocation loops and voids. In contrast, the hardness of the AGIR sample remained almost unchanged due to the combined effect of nanoprecipitates evolution and voids elimination. The strength contributions calculated by DBH model have a good qualitative correspondence with the hardness measured by experiment.
- (3) The swelling rate of cobalt-free MEAs can be effectively controlled by the trapping relationship between the L_1_2 nanoprecipitates and voids, as well as the precipitation and dissolution transition of nanoprecipitates. The SSIR sample shows lowest swelling rate ($9.4 \times 10^{-6} \text{ %/dpa}$) than most other HEAs/steels. Furthermore, the AGIR sample presents an even better radiation tolerance with no swelling under the same irradiation condition.

CRediT authorship contribution statement

Jihong Han: Conceptualization, Methodology, Software, Writing – original draft. **Yang Zhang:** Methodology, Supervision, Writing – review & editing, Funding acquisition. **Zhiyan Sun:** Data curation, Writing – review & editing. **Yunfei Zhang:** Data curation, Writing – review & editing. **Yingli Zhao:** Data curation, Writing – review & editing. **Lixin Sun:** Funding acquisition, Writing – review & editing. **Zhongwu Zhang:** Supervision, Funding acquisition, Writing – review & editing.

Declaration of Competing Interest

The authors declare that they have no known competing financial interests or personal relationships that could have appeared to influence the work reported in this paper.

Data availability

Data will be made available on request.

Acknowledgments

The present work is supported by the NSFC Funding (U2141207, 52001083, 52171111), Key Laboratory Found of the Ministry of Industry and Information Technology (GXB202205), Youth Talent Project

of China National Nuclear Corporation (CNNC2021YTEP-HEU01), and China-Ukraine Intergovernmental Science and Technology Exchange Project (G4822007).

References

- [1] Y. Cui, E. Aydogan, J.G. Gigax, Y. Wang, A. Misra, S.A. Maloy, N. Li, *In situ* micropillar compression to examine radiation-induced hardening mechanisms of FeCrAl alloys, *Acta Mater.* 202 (2021) 255–265.
- [2] Y. Li, G. Ran, X. Liu, Q. Han, X. Huang, Y. Ding, *In-situ* TEM investigation of dislocation loop reaction and irradiation hardening in H₂⁺ - He⁺ dual-beam irradiated Mo, *J. Mater. Sci. Technol.* 107 (2022) 14–25.
- [3] S. Jiang, C. Yu, P. Zheng, L. Guo, X. Zhou, W.F. Rao, Bubbles and precipitates formation and effects on the hardening of irradiated vanadium alloys, *J. Nucl. Mater.* 544 (2021).
- [4] K. Jin, C. Lu, L.M. Wang, J. Qu, W.J. Weber, Y. Zhang, H. Bei, Effects of compositional complexity on the ion-irradiation induced swelling and hardening in Ni-containing equiatomic alloys, *Scr. Mater.* 119 (2016) 65–70.
- [5] K.i. Fukumoto, T. Mabuchi, K. Yabuuchi, K. Fujii, Irradiation hardening of stainless steel model alloy after Fe-ion irradiation and post-irradiation annealing treatment, *J. Nucl. Mater.* 557 (2021).
- [6] N. Almirall, P.B. Wells, T. Yamamoto, K. Wilford, T. Williams, N. Riddle, G. R. Odette, Precipitation and hardening in irradiated low alloy steels with a wide range of Ni and Mn compositions, *Acta Mater.* 179 (2019) 119–128.
- [7] A. Kamboj, M.N. Bachhav, M. Dubey, N. Almirall, T. Yamamoto, E.A. Marquis, G. R. Odette, The effect of phosphorus on precipitation in irradiated reactor pressure vessel (RPV) steels, *J. Nucl. Mater.* 585 (2023).
- [8] G.R. Odette, N. Almirall, P.B. Wells, T. Yamamoto, Precipitation in reactor pressure vessel steels under ion and neutron irradiation: on the role of segregated network dislocations, *Acta Mater.* 212 (2021).
- [9] G.R. Odette, M.J. Alinger, B.D. Wirth, Recent developments in irradiation-resistant steels, *Annu. Rev. Mater. Res.* 38 (1) (2008) 471–503.
- [10] A.M. Robinson, P.D. Edmondson, C. English, S. Lozano-Perez, G. Greaves, J. A. Hinks, S.E. Donnelly, C.R.M. Grovenor, The effect of temperature on bubble lattice formation in copper under *in situ* He ion irradiation, *Scr. Mater.* 131 (2017) 108–111.
- [11] J. Wen, C. Sun, P.P. Dholabhai, Y. Xia, M. Tang, D. Chen, D.Y. Yang, Y.H. Li, B. P. Uberuaga, Y.Q. Wang, Temperature dependence of the radiation tolerance of nanocrystalline pyrochlores A₂Ti₂O₇ (A = Gd, Ho and Lu), *Acta Mater.* 110 (2016) 175–184.
- [12] Z. Chen, L.L. Niu, Z. Wang, L. Tian, L. Kecskes, K. Zhu, Q. Wei, A comparative study on the *in situ* helium irradiation behavior of tungsten: coarse grain vs. nanocrystalline grain, *Acta Mater.* 147 (2018) 100–112.
- [13] S.J. Zinkle, L.L. Snead, Designing radiation resistance in materials for fusion energy, *Annu. Rev. Mater. Res.* 44 (1) (2014) 241–267.
- [14] H. Wang, F. Ren, J. Tang, W. Qin, L. Hu, L. Dong, B. Yang, G. Cai, C. Jiang, Enhanced radiation tolerance of YSZ/Al₂O₃ multilayered nanofilms with pre-existing nanovoids, *Acta Mater.* 144 (2018) 691–699.
- [15] C. Lu, T. Yang, K. Jin, N. Gao, P. Xiu, Y. Zhang, F. Gao, H. Bei, W.J. Weber, K. Sun, Y. Dong, L. Wang, Radiation-induced segregation on defect clusters in single-phase concentrated solid-solution alloys, *Acta Mater.* 127 (2017) 98–107.
- [16] N.A.P.K. Kumar, C. Li, K.J. Leonard, H. Bei, S.J. Zinkle, Microstructural stability and mechanical behavior of FeNiMnCr high entropy alloy under ion irradiation, *Acta Mater.* 113 (2016) 230–244.
- [17] J. Gan, E.P. Simonen, S.M. Bruemmer, L. Fournier, B.H. Sencer, G.S. Was, The effect of oversized solute additions on the microstructure of 316SS irradiated with 5 MeV Ni⁺ ions or 3.2 MeV protons, *J. Nucl. Mater.* 325 (2–3) (2004) 94–106.
- [18] T. Okita, T. Sato, N. Sekimura, T. Iwai, F.A. Garner, The synergistic influence of temperature and displacement rate on microstructural evolution of ion-irradiated Fe-15Cr-16Ni model austenitic alloy, *J. Nucl. Mater.* 367–370 (2007) 930–934.
- [19] T. Yang, W. Guo, J.D. Poplawsky, D. Li, L. Wang, Y. Li, W. Hu, M.L. Crespillo, Z. Yan, Y. Zhang, Y. Wang, S.J. Zinkle, Structural damage and phase stability of Al_{0.3}CoCrFeNi high entropy alloy under high temperature ion irradiation, *Acta Mater.* 188 (2020) 1–15.
- [20] S.J. Zinkle, G.S. Was, Materials challenges in nuclear energy, *Acta Mater.* 61 (3) (2013) 735–758.
- [21] C. Lu, L. Niu, N. Chen, K. Jin, T. Yang, P. Xiu, Y. Zhang, F. Gao, H. Bei, S. Shi, M. R. He, I.M. Robertson, W.J. Weber, L. Wang, Enhancing radiation tolerance by controlling defect mobility and migration pathways in multicomponent single-phase alloys, *Nat. Commun.* 7 (2016) 13564.
- [22] Y. Zhang, W.Q. Jiang, A. Gokman, J.J. Yang, K. Shi, J.H. Luan, Y. Cui, P.K. Liaw, C.T. Liu, Z.W. Zhang, Enhanced irradiation tolerance of Fe₃₀Cr₂₅Ni₂₀Co₁₅Mn₁₀ high-entropy alloy via nanowin boundaries, *J. Nucl. Mater.* 557 (2021).
- [23] T.X. Li, J.W. Miao, E.Y. Guo, H. Huang, J. Wang, Y.P. Lu, T.M. Wang, Z.Q. Cao, T. J. Li, Tungsten-containing high-entropy alloys: a focused review of manufacturing routes, phase selection, mechanical properties, and irradiation resistance properties, *Tungsten* 3 (2) (2021) 181–196.
- [24] X. Wang, H. Huang, J. Shi, H.Y. Xu, D.Q. Meng, Recent progress of tungsten-based high-entropy alloys in nuclear fusion, *Tungsten* 3 (2) (2021) 143–160.
- [25] Y. Zhang, G.M. Stocks, K. Jin, C. Lu, H. Bei, B.C. Sales, L. Wang, L.K. Beland, R. E. Stoller, G.D. Samolyuk, M. Caro, A. Caro, W.J. Weber, Influence of chemical disorder on energy dissipation and defect evolution in concentrated solid solution alloys, *Nat. Commun.* 6 (2015) 8736.
- [26] M.R. He, S. Wang, K. Jin, H. Bei, K. Yasuda, S. Matsumura, K. Higashida, I. M. Robertson, Enhanced damage resistance and novel defect structure of CrFeCoNi under *in situ* electron irradiation, *Scr. Mater.* 125 (2016) 5–9.
- [27] T.N. Yang, C. Lu, G. Velisa, K. Jin, P. Xiu, Y. Zhang, H. Bei, L. Wang, Influence of irradiation temperature on void swelling in NiCoFeCrMn and NiCoFeCrPd, *Scr. Mater.* 158 (2019) 57–61.
- [28] Z. Cheng, J. Sun, X. Gao, Y. Wang, J. Cui, T. Wang, H. Chang, Irradiation effects in high-entropy alloys and their applications, *J. Alloy. Compd.* 930 (2023).
- [29] B. Kombaiah, K. Jin, H. Bei, P.D. Edmondson, Y. Zhang, Phase stability of single phase Al_{0.12}CrNiFeCo high entropy alloy upon irradiation, *Mater. Des.* 160 (2018) 1208–1216.
- [30] W.Y. Chen, M.A. Kirk, N. Hashimoto, J.W. Yeh, X. Liu, Y. Chen, Irradiation effects on Al_{0.3}CoCrFeNi and CoCrMnFeNi high-entropy alloys, and 316H stainless steel at 500°C, *J. Nucl. Mater.* 539 (2020).
- [31] Y.L. Zhao, F.L. Meng, T. Yang, J.H. Luan, S.F. Liu, G.M. Yeli, W.T. Lin, W.H. Liu, X.J. Liu, C.T. Liu, J.J. Kai, Enhanced helium ion irradiation tolerance in a Fe-Co-Ni-Cr-Al-Ti high-entropy alloy with Li₂ nanoparticles, *J. Mater. Sci. Technol.* 143 (2023) 169–177.
- [32] M.R. He, S. Wang, S. Shi, K. Jin, H. Bei, K. Yasuda, S. Matsumura, K. Higashida, I. M. Robertson, Mechanisms of radiation-induced segregation in CrFeCoNi-based single-phase concentrated solid solution alloys, *Acta Mater.* 126 (2017) 182–193.
- [33] T. Yang, Y.L. Zhao, W.H. Liu, J.H. Zhu, J.J. Kai, C.T. Liu, Ductilizing brittle high-entropy alloys via tailoring valence electron concentrations of precipitates by controlled elemental partitioning, *Mater. Res. Lett.* 6 (10) (2018) 600–606.
- [34] L. Liu, Y. Zhang, J. Li, M. Fan, X. Wang, G. Wu, Z. Yang, J. Luan, Z. Jiao, C.T. Liu, P.K. Liaw, Z. Zhang, Enhanced strength-ductility synergy via novel bifunctional nano-precipitates in a high-entropy alloy, *Int. J. Plast.* 153 (2022).
- [35] B. Xiao, J. Luan, S. Zhao, L. Zhang, S. Chen, Y. Zhao, L. Xu, C.T. Liu, J.J. Kai, T. Yang, Achieving thermally stable nanoparticles in chemically complex alloys via controllable sluggish lattice diffusion, *Nat. Commun.* 13 (1) (2022) 4870.
- [36] G. Yeli, D. Chen, K. Yabuuchi, A. Kimura, S. Liu, W. Lin, Y. Zhao, S. Zhao, J.J. Kai, The stability of γ' precipitates in a multi-component FeCoNiCrTi_{0.2} alloy under elevated-temperature irradiation, *J. Nucl. Mater.* 540 (2020).
- [37] Y. Zhao, A. Bhattacharya, C. Pareige, C. Massey, P. Zhu, J.D. Poplawsky, J. Henry, S.J. Zinkle, Effect of heavy ion irradiation dose rate and temperature on α' precipitation in high purity Fe-18%Cr alloy, *Acta Mater.* 231 (2022).
- [38] W.Y. Chen, X. Liu, Y. Chen, J.W. Yeh, K.K. Tseng, K. Natesan, Irradiation effects in high entropy alloys and 316H stainless steel at 300 °C, *J. Nucl. Mater.* 510 (2018) 421–430.
- [39] Z. Su, T. Shi, J. Yang, H. Shen, Z. Li, S. Wang, G. Ran, C. Lu, The effect of interstitial carbon atoms on defect evolution in high entropy alloys under helium irradiation, *Acta Mater.* 233 (2022).
- [40] A. Hussain, S.A. Khan, S.K. Sharma, K. Sudarshan, S.K. Sharma, C. Singh, P. K. Kulriya, Influence of defect dynamics on the nanoindentation hardness in NiCoCrFePd high entropy alloy under high dose Xe⁺³ irradiation, *Mater. Sci. Eng. A* 863 (2023).
- [41] S. Shen, F. Chen, X. Tang, J. Lin, G. Ge, J. Liu, Effects of carbon doping on irradiation resistance of Fe₃₈Mn₄₀Ni₁₁Al₄Cr₇ high entropy alloys, *J. Nucl. Mater.* 540 (2020).
- [42] J. Du, S. Jiang, P. Cao, C. Xu, Y. Wu, H. Chen, E. Fu, Z. Lu, Superior radiation tolerance via reversible disordering-ordering transition of coherent superlattices, *Nat. Mater.* (2022).
- [43] P.P. Cao, H. Wang, J.Y. He, C. Xu, S.H. Jiang, J.L. Du, X.Z. Cao, E.G. Fu, Z.P. Lu, Effects of nanosized precipitates on irradiation behavior of CoCrFeNi high entropy alloys, *J. Alloy. Compd.* 859 (2021).
- [44] Y.L. Zhao, T. Yang, J.H. Zhu, D. Chen, Y. Yang, A. Hu, C.T. Liu, J.J. Kai, Development of high-strength Co-free high-entropy alloys hardened by nanosized precipitates, *Scr. Mater.* 148 (2018) 51–55.
- [45] J. Han, Y. Zhang, Z. Zhang, L. Liu, J. Li, Y. Yu, L. Sun, Strength-plasticity regulation via nanoscale precipitation and coprecipitation in cobalt-free medium-entropy alloys, *Mater. Charact.* 193 (2022).
- [46] Z. Wu, H. Bei, Microstructures and mechanical properties of compositionally complex Co-free FeNiMnCr₁₈ FCC solid solution alloy, *Mater. Sci. Eng. A* 640 (2015) 217–224.
- [47] P. Hosemann, D. Frazer, M. Fratoni, A. Bolind, M.F. Ashby, Materials selection for nuclear applications: challenges and opportunities, *Scr. Mater.* 143 (2018) 181–187.
- [48] A. Takeuchi, A. Inoue, Classification of bulk metallic glasses by atomic size difference, heat of mixing and period of constituent elements and its application to characterization of the main alloying element, *Mater. Trans.* 46 (12) (2005) 2817–2829.
- [49] L. Liu, Y. Zhang, J. Han, X. Wang, W. Jiang, C.T. Liu, Z. Zhang, P.K. Liaw, Nanoprecipitate-strengthened high-entropy alloys, *Adv. Sci.* 8 (23) (2021).
- [50] L. Fan, T. Yang, J.H. Luan, Z.B. Jiao, Control of discontinuous and continuous precipitation of γ' -strengthened high-entropy alloys through nanoscale Nb segregation and partitioning, *J. Alloy. Compd.* 832 (2020).
- [51] S. Guo, C. Ng, J. Lu, C.T. Liu, Effect of valence electron concentration on stability of fcc or bcc phase in high entropy alloys, *J. Appl. Phys.* 109 (10) (2011).
- [52] G. Laplanche, P. Gadaud, C. Bärsch, K. Demtröder, C. Reinhart, J. Schreuer, E. P. George, Elastic moduli and thermal expansion coefficients of medium-entropy subsystems of the CrMnFeCoNi high-entropy alloy, *J. Alloy. Compd.* 746 (2018) 244–255.
- [53] Z. Wu, H. Bei, F. Otto, G.M. Pharr, E.P. George, Recovery, recrystallization, grain growth and phase stability of a family of FCC-structured multi-component equiatomic solid solution alloys, *Intermetallics* 46 (2014) 131–140.

- [54] M. Schneider, G. Laplanche, Effects of temperature on mechanical properties and deformation mechanisms of the equiatomic CrFeNi medium-entropy alloy, *Acta Mater.* 204 (2021).
- [55] L. Tang, F.Q. Jiang, J.S. Wróbel, B. Liu, S. Kabra, R.X. Duan, J.H. Luan, Z.B. Jiao, M.M. Attallah, D. Nguyen-Manh, B. Cai, In situ neutron diffraction unravels deformation mechanisms of a strong and ductile FeCrNi medium entropy alloy, *J. Mater. Sci. Technol.* 116 (2022) 103–120.
- [56] Y. Iwamoto, H. Iwamoto, M. Harada, K. Niita, Calculation of displacement cross-sections for structural materials in accelerators using PHITS event generator and its applications to radiation damage, *J. Nucl. Sci. Technol.* 51 (1) (2013) 98–107.
- [57] Y. Kudriavtsev, A. Villegas, A. Godines, R. Asomoza, Calculation of the surface binding energy for ion sputtered particles, *Appl. Surf. Sci.* 239 (3–4) (2005) 273–278.
- [58] R.E. Stoller, M.B. Toloczko, G.S. Was, A.G. Certain, S. Dwaraknath, F.A. Garner, On the use of SRIM for computing radiation damage exposure, *Nucl. Instrum. Methods Phys. Res. Sect. B Beam Interact. Mater. Atoms* 310 (2013) 75–80.
- [59] J.Y. He, H. Wang, H.L. Huang, X.D. Xu, M.W. Chen, Y. Wu, X.J. Liu, T.G. Nieh, K. An, Z.P. Lu, A precipitation-hardened high-entropy alloy with outstanding tensile properties, *Acta Mater.* 102 (2016) 187–196.
- [60] Y.L. Zhao, Y.R. Li, G.M. Yeli, J.H. Luan, S.F. Liu, W.T. Lin, D. Chen, X.J. Liu, J. Kai, C.T. Liu, T. Yang, Anomalous precipitate-size-dependent ductility in multicomponent high-entropy alloys with dense nanoscale precipitates, *Acta Mater.* 223 (2022).
- [61] B.X. Cao, T. Yang, L. Fan, J.H. Luan, Z.B. Jiao, C.T. Liu, Refractory alloying additions on the thermal stability and mechanical properties of high-entropy alloys, *Mater. Sci. Eng. A* 797 (2020).
- [62] S. Shu, N. Almirall, P.B. Wells, T. Yamamoto, G.R. Odette, D.D. Morgan, Precipitation in Fe-Cu and Fe-Cu-Mn model alloys under irradiation: dose rate effects, *Acta Mater.* 157 (2018) 72–82.
- [63] M. Mamivand, Y. Yang, J. Busby, D. Morgan, Integrated modeling of second phase precipitation in cold-worked 316 stainless steels under irradiation, *Acta Mater.* 130 (2017) 94–110.
- [64] M. Song, Y. Yang, M. Wang, W. Kuang, C.R. Lear, G.S. Was, Probing long-range ordering in nickel-base alloys with proton irradiation, *Acta Mater.* 156 (2018) 446–462.
- [65] M. Seyring, M. Rettenmayr, Impact of crystallography at Ni/NiAl interfaces on the nucleation of Ni₃Al, *Acta Mater.* 208 (2021).
- [66] Y.Q. Chen, T.J. Slater, E.A. Lewis, E.M. Francis, M.G. Burke, M. Preuss, S.J. Haigh, Measurement of size-dependent composition variations for gamma prime (γ') precipitates in an advanced nickel-based superalloy, *Ultramicroscopy* 144 (2014) 1–8.
- [67] G.A. Young, J.D. Tucker, D.R. Eno, The kinetics of long range ordering in Ni-Cr and Ni-Cr-Fe alloys, in: Proceedings of the 16th Annual Conference on the Environmentally Assisted Cracking of Materials in Nuclear Power Systems-Water Reactors, 2013, pp. 1–22.
- [68] T. Yang, Y.L. Zhao, L. Fan, J. Wei, J.H. Luan, W.H. Liu, C. Wang, Z.B. Jiao, J. Kai, C.T. Liu, Control of nanoscale precipitation and elimination of intermediate-temperature embrittlement in multicomponent high-entropy alloys, *Acta Mater.* 189 (2020) 47–59.
- [69] G. Neumann, C. Tuijn, Self-Diffusion and Impurity Diffusion in Pure Metals: Handbook of Experimental Data, Elsevier, 2011.
- [70] Y.Y. Zhao, H.W. Chen, Z.P. Lu, T.G. Nieh, Thermal stability and coarsening of coherent particles in a precipitation-hardened (NiCoFeCr)₉₄Ti₂Al₄ high-entropy alloy, *Acta Mater.* 147 (2018) 184–194.
- [71] L. He, L. Tan, Y. Yang, K. Sridharan, Evolution of B₂ and laves phases in a ferritic steel under Fe²⁺ ion irradiation at 475°C, *J. Nucl. Mater.* 525 (2019) 102–110.
- [72] M.L. Lescot, J. Ribis, Y. Chen, E. Marquis, E. Bordas, P. Trocellier, Y. Serruys, A. Gentilis, O. Kaïtasov, Y. De Carlan, Radiation-induced Ostwald ripening in oxide dispersion strengthened ferritic steels irradiated at high ion dose, *Acta Mater.* 78 (2014) 328–340.
- [73] Y. Zhang, L. Liu, J. Han, J. Yang, J. Luan, Z. Jiao, C.T. Liu, Z. Zhang, Irradiation-induced solute trapping by preexisting nanoprecipitates in high-strength low-alloy steel, *Mater. Sci. Eng. A* 849 (2022).
- [74] Z.W. Zhang, C.T. Liu, X.L. Wang, M.K. Miller, D. Ma, G. Chen, J.R. Williams, B. A. Chin, Effects of proton irradiation on nanocluster precipitation in ferritic steel containing fcc alloying additions, *Acta Mater.* 60 (6–7) (2012) 3034–3046.
- [75] P. Changizian, Z. Yao, C. Lu, F. Long, M.R. Daymond, Radiation effect on nanoindentation properties and deformation mechanisms of a Ni-based superalloy X-750, *J. Nucl. Mater.* 515 (2019) 1–13.
- [76] K. Jin, Y.F. Gao, H. Bei, Intrinsic properties and strengthening mechanism of monocrystalline Ni-containing ternary concentrated solid solutions, *Mater. Sci. Eng. A* 695 (2017) 74–79.
- [77] D. Wang, L. Zhao, L. Xu, Y. Han, K. Hao, A microstructure-based study of irradiation hardening in stainless steel: experiment and phase field modeling, *J. Nucl. Mater.* 569 (2022).
- [78] T. Chen, L. He, M.H. Cullison, C. Hay, J. Burns, Y. Wu, L. Tan, The correlation between microstructure and nanoindentation property of neutron-irradiated austenitic alloy D9, *Acta Mater.* 195 (2020) 433–445.
- [79] L. Tan, J.T. Busby, Formulating the strength factor α for improved predictability of radiation hardening, *J. Nucl. Mater.* 465 (2015) 724–730.
- [80] Z.F. Wu, L.D. Xu, H.Q. Chen, Y.X. Liang, J.L. Du, Y.F. Wang, S.L. Zhang, X.C. Cai, B.R. Sun, J. Zhang, T.D. Shen, J. Wang, E.G. Fu, Significant suppression of void swelling and irradiation hardening in a nanogranulated/nanoprecipitated 14YWT-ODS steel irradiated by helium ions, *J. Nucl. Mater.* 559 (2022).
- [81] M.C. Niu, L.C. Yin, K. Yang, J.H. Luan, W. Wang, Z.B. Jiao, Synergistic alloying effects on nanoscale precipitation and mechanical properties of ultrahigh-strength steels strengthened by Ni₃Ti, Mo-enriched, and Cr-rich co-precipitates, *Acta Mater.* 209 (2021).
- [82] C.A. Dennett, K.P. So, A. Fukushima, D.L. Buller, K. Hattar, M.P. Short, Detecting self-ion irradiation-induced void swelling in pure copper using transient grating spectroscopy, *Acta Mater.* 145 (2018) 496–503.
- [83] X. Wang, A.M. Monterrosa, F. Zhang, H. Huang, Q. Yan, Z. Jiao, G.S. Was, L. Wang, Void swelling in high dose ion-irradiated reduced activation ferritic-martensitic steels, *J. Nucl. Mater.* 462 (2015) 119–125.
- [84] K. Yabuuchi, R. Kasada, A. Kimura, Effect of alloying elements on irradiation hardening behavior and microstructure evolution in BCC Fe, *J. Nucl. Mater.* 442 (1–3) (2013) S790–S795.
- [85] D. Gelles, Void swelling in binary FeCr alloys at 200 dpa, *J. Nucl. Mater.* 225 (1995) 163–174.
- [86] M. Klimenkov, A. Möslang, E. Materna-Morris, Helium influence on the microstructure and swelling of 9%Cr ferritic steel after neutron irradiation to 16.3 dpa, *J. Nucl. Mater.* 453 (1–3) (2014) 54–59.
- [87] L. Shao, C.C. Wei, J. Gigax, A. Aitkaliyeva, D. Chen, B.H. Sencer, F.A. Garner, Effect of defect imbalance on void swelling distributions produced in pure iron irradiated with 3.5 MeV self-ions, *J. Nucl. Mater.* 453 (1–3) (2014) 176–181.
- [88] M.B. Toloczko, F.A. Garner, V.N. Voyevodin, V.V. Bryk, O.V. Borodin, V. V. Mel'nychenko, A.S. Kalchenko, Ion-induced swelling of ODS ferritic alloy MA957 tubing to 500 dpa, *J. Nucl. Mater.* 453 (1–3) (2014) 323–333.
- [89] E. Getto, Z. Jiao, A.M. Monterrosa, K. Sun, G.S. Was, Effect of pre-implanted helium on void swelling evolution in self-ion irradiated HT9, *J. Nucl. Mater.* 462 (2015) 458–469.
- [90] E. Getto, Z. Jiao, A.M. Monterrosa, K. Sun, G.S. Was, Effect of irradiation mode on the microstructure of self-ion irradiated ferritic-martensitic alloys, *J. Nucl. Mater.* 465 (2015) 116–126.
- [91] T. Chen, E. Aydogan, J.G. Gigax, D. Chen, J. Wang, X. Wang, S. Ukai, F.A. Garner, L. Shao, Microstructural changes and void swelling of a 12Cr ODS ferritic-martensitic alloy after high-dpa self-ion irradiation, *J. Nucl. Mater.* 467 (2015) 42–49.
- [92] E. Getto, K. Sun, A.M. Monterrosa, Z. Jiao, M.J. Hackett, G.S. Was, Void swelling and microstructure evolution at very high damage level in self-ion irradiated ferritic-martensitic steels, *J. Nucl. Mater.* 480 (2016) 159–176.
- [93] G. Meric de Bellfon, K.M. Bertsch, M.R. Chancey, Y.Q. Wang, D.J. Thoma, Influence of solidification structures on radiation-induced swelling in an additively-manufactured austenitic stainless steel, *J. Nucl. Mater.* 523 (2019) 291–298.
- [94] L. Jiang, M. Song, L. Yang, J. Yang, D. Du, X. Lou, Y. Chen, A comparison study of void swelling in additively manufactured and cold-worked 316L stainless steels under ion irradiation, *J. Nucl. Mater.* 551 (2021).
- [95] A. Gabriel, L. Hawkins, A. French, Y. Li, Z. Hu, L. He, P. Xiu, M. Nastasi, F. A. Garner, L. Shao, Effect of dpa rate on the temperature regime of void swelling in ion-irradiated pure chromium, *J. Nucl. Mater.* 561 (2022).
- [96] M. Moschetti, P.A. Burr, E. Obbard, J.J. Krueck, P. Hosemann, B. Gludovatz, Design considerations for high entropy alloys in advanced nuclear applications, *J. Nucl. Mater.* 567 (2022).
- [97] H. Kim, J.G. Gigax, O. El-Atwani, M.R. Chancey, J.K. Baldwin, Y. Wang, S. A. Maloy, Comparison of void swelling of ferritic-martensitic and ferritic HT9 alloys after high-dose self-ion irradiation, *Mater. Charact.* 173 (2021).
- [98] M. Song, Y.D. Wu, D. Chen, X.M. Wang, C. Sun, K.Y. Yu, Y. Chen, L. Shao, Y. Yang, K.T. Hartwig, X. Zhang, Response of equal channel angular extrusion processed ultrafine-grained T91 steel subjected to high temperature heavy ion irradiation, *Acta Mater.* 74 (2014) 285–295.
- [99] O. El-Atwani, E. Esquivel, M. Efe, E. Aydogan, Y.Q. Wang, E. Martinez, S. A. Maloy, Loop and void damage during heavy ion irradiation on nanocrystalline and coarse grained tungsten: microstructure, effect of dpa rate, temperature, and grain size, *Acta Mater.* 149 (2018) 206–219.
- [100] Y.R. Lin, A. Bhattacharya, D. Chen, J.J. Kai, J. Henry, S.J. Zinkle, Temperature-dependent cavity swelling in dual-ion irradiated Fe and Fe-Cr ferritic alloys, *Acta Mater.* 207 (2021).
- [101] Q. Liu, S. Xia, Y. Su, J. Huang, S. Zhao, F. Luo, H. Liu, W. Ge, J. Xue, C. Wang, Y. Wang, Enhanced recombination suppresses the void swelling in bcc multi-component alloys, *Materialia* 20 (2021).